

# Study of orbital and superorbital variability of LSI +61° 303 with X-ray data

M. Chernyakova<sup>1,2</sup>, Iu. Babyk<sup>1,2,3,8</sup>, D. Malyshev<sup>4</sup>, Ie. Vovk<sup>5</sup>, S. Tsygankov<sup>6</sup>,  
H. Takahashi<sup>7</sup>, Ya. Fukazawa<sup>7</sup>

<sup>1</sup> School of Physical Sciences, Dublin City University, Dublin 9, Ireland

<sup>2</sup> Dublin Institute for Advanced Studies, 31 Fitzwilliam Place, Dublin 2, Ireland

<sup>3</sup> University of Waterloo, 200 University Ave W, Waterloo, Ontario, N2L 3G1, Canada

<sup>4</sup> Institut für Astronomie und Astrophysik Tübingen, Universität Tübingen, Sand 1, D-72076 Tübingen, Germany

<sup>5</sup> Max Planck Institute for Physics, Föhringer Ring 6, 80805 Munich, Germany

<sup>6</sup> Tuorla Observatory, Department of Physics and Astronomy, University of Turku, Väisäläntie 20, FI-21500, Piikkiö, Finland

<sup>7</sup> Department of Physical Science, Hiroshima University, 1-3-1 Kagamiyama, Higashi-Hiroshima, Hiroshima, 739-8526, Japan

<sup>8</sup> Main Astronomical Observatory of National Academy of Science of Ukraine, Academica Zabolotnogo str., 27, Kyiv, 03143, Ukraine

Received <date> ; in original form <date>

## ABSTRACT

LSI +61° 303 is one of the few X-ray binaries with a Be star companion from which radio, X-rays and high-energy gamma-ray (GeV and TeV) emission have been observed. The nature of the high energy activity of the system is not yet fully understood, but it is widely believed that it is generated due to the interaction of the relativistic electrons leaving the compact object with the photons and non-relativistic wind of the Be star. The superorbital variability of the system has been observed in the radio, optical and X-ray domains and could be due to the cyclic change of the Be star disk size. In this paper we systematically review all publicly available data from *Suzaku*, *XMM-Newton*, *Chandra* and *Swift* observatories in order to measure the absorption profile of the circumstellar Be disk as a function of orbital and superorbital phases. We also discuss short-term variability of the system, found during the analysis and its implications for the understanding of the physical processes in this system.

**Key words:** X-rays: binaries – X-rays: individual: LSI +61° 303

## 1 INTRODUCTION

LSI +61° 303 is one of the few X-ray binaries observed from the radio to very high-energy gamma-ray bands. It consists of a Be star and a compact object on an eccentric orbit (see Fig. 1). The nature of the compact object is not known due to poor constraints on its mass implied by large uncertainty of the inclination angle (see, e.g., Sierpowska-Bartosik & Torres 2009; Caliendo, Torres & Rea 2012).

The radio observations of LSI +61° 303 cover more than two decades and demonstrate that the observed emission is modulated on timescales of  $\sim 26.5$  d and  $\sim 1667$  d (Gregory 2002). These timescales are usually interpreted as the orbital and superorbital periods of the system (see, however, Massi & Jaron (2013); Massi, Jaron & Hovatta (2015)). The detection of similar periods has been recently reported in the optical (Zamanov et al. 2013; Paredes-Fortuny et al. 2015), X-ray (Chernyakova et al. 2012; Li, Torres & Zhang 2014) and gamma-ray bands (Ackermann et al. 2013; Jaron & Massi 2014).

The nature of the superorbital period is not well established. Chernyakova et al. (2012) found that while both, X-ray and radio, lightcurves of LSI +61° 303 demonstrate one peak per orbit (with

the position of orbital phase modulated on the superorbital scale), the X-ray peak systematically outruns the radio one by about  $\sim 5.3$  days. The observed behaviour was interpreted in terms of separate radio and X-ray emission regions. In the dense region of the Be star's equatorial disk, the interaction of the compact object with the wind leads to the injection of high-energy particles into the wind. These particles escape from the system with the stellar wind velocity. While the X-ray emission can be observed even if it is generated within the system, the radio emission from particles located closer than  $\sim 5 \times 10^{13}$  cm to the Be star, is heavily absorbed (Zdziarski, Neronov & Chernyakova 2010). The observed phase lag between X-ray and radio maxima corresponds to the escape time of the high-energy particles from the system with the stellar wind. The superorbital period in this model is connected with the processes of gradual build-up and decay of the Be star disk. Shortly after the superorbital phase  $\Phi \sim 0.6$ , the disk is weak and can be easily perturbed and partially striped away by a relativistic outflow from a compact object resulting in a narrow, pronounced X-ray peak. The gradual build-up of the disk up to the superorbital phase  $\Phi \sim 0.6$  leads to an increase of the time that the compact object spend in dense regions of the disk and thus to the broadening and blurring of the observed X-ray maximum.

The optical (continuum and  $H\alpha$  line) observations of LSI +61° 303 by Zamanov et al. (2013); Paredes-Fortuny et al. (2015) have also revealed the variability of the system on orbital and superorbital timescales. It was found, that the orbital position of the maximum equivalent width of the  $H\alpha$  emission line, and the radius of the disk, peak after periastron and coincide on average with the X-ray and  $\gamma$ -ray maxima.

Another bit of information regarding the disk size/density profile can be obtained from low-energy photoelectric absorption in X-rays. Indeed, if the superorbital variability in the system is linked with the disk build-up process (e.g. Chernyakova et al. (2012)) one can expect the gradual increase of the absorption, as the compact object moves on its orbit.

Below we present an attempt to measure the absorption profile of the circumstellar Be disk as a function of orbital and superorbital phases, based on all available X-ray observations of LSI +61° 303. We also discuss short-term variability of the system, found during the analysis and its implications for the understanding of the physical processes in this system.

## 2 DATA ANALYSIS

Hereafter, we adopt the following parameters for the LSI +61° 303 system – the orbital and superorbital periods  $P_{orb} = 26.496 \pm 0.0028$  d and  $P_{so} = 1667$  d are from Gregory (2002). The values for the eccentricity of  $e = 0.537 \pm 0.034$  and the phase of the periastron of  $\varphi = 0.275 \pm 0.010$  are adopted from Aragona et al. (2009). Historically the phase of  $\varphi = 0$  corresponds to Julian Date (JD) 2,443,366.775 (Gregory 2002).

In this work we use all publicly available *Suzaku*, *XMM-Newton*, *Chandra* and *Swift* data. Graphical representation of the orbital position of all the observations is given in Fig. 1. To quantitatively characterise the short time scale variability observed at different observations we have calculated the root-mean-square function (RMS) for each light curve. To calculate it we have used a standard definition of

$$RMS = \sqrt{\frac{\sum (f_i - \langle f \rangle)^2}{N}}, \quad (1)$$

where  $N$  is the full number of time bins in the light curve, and  $\langle f \rangle = \sum (f_i \delta f_i^{-2}) / \sum (\delta f_i^{-2})$  is the weighted mean of the flux with the error of  $\delta f_i$  for each time bin  $t_i$  with a flux  $f_i$ . For consistency we used throughout the paper a time bin size of 1 ks in all the observations, and the corresponded RMS is denoted as  $RMS_{1ks}$ .

### 2.1 *Suzaku* observations

In 2009 *Suzaku* performed three long ( $\sim 170$  ks in total) observations of LSI +61° 303 (see Table 1). All these observations occurred within the same orbital cycle. One (S3) happens to be near the periastron and the other two are close to apastron.

The *Suzaku* observations were performed with the X-ray Imaging Spectrometer (XIS; Koyama et al. (2007)) in the spectral range 0.3 – 12 keV and the hard X-ray detector (HXD; Takahashi et al. (2007)) at 13 – 600 keV. The X-ray imaging spectrometers are located at the focal plane of the XRT and consist of one back-illuminated CCD camera (XIS-1) and three front-illuminated CCDs (XIS-0, -2, and -3). After a fatal damage on 2006 November 9 XIS-2 becomes unusable.

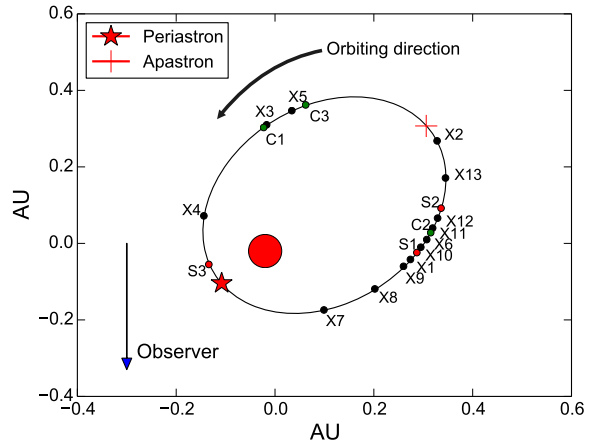


**Figure 1.** Orbital geometry of LSI +61° 303 adapted from Aragona et al. (2009), along with the positions during *Suzaku* (S), *XMM-Newton* (X), and *Chandra* (C) observations.

**Table 1.** Log of *Suzaku* data.  $\phi$  and  $\Phi$  are orbital and superorbital phases correspondingly.

Obs. date	ObsID	Ref	MJD	Exp. time ks	$\phi$	$\Phi$
22-01-2009	403015010	S1	54853.951	40.5	0.562	0.8912
25-01-2009	403016010	S2	54856.696	61.0	0.666	0.8928
10-02-2009	403017010	S3	54872.184	68.6	0.251	0.9021

Data reduction was done using HEASoft<sup>1</sup> v.6.16 software package, while spectral modelling was performed in XSpec environment v.12.8.2.

For XIS data, we performed full XIS reprocessing and screening data using the AEPipeline tool. The processing pipeline V2.1.6.16 was used to process data sets. In our analysis we used cleaned event files, with standard screening applied. The source photons were extracted from a circular area with a 3 arc minute radius. The background photons were taken from a circle with the same radius from a nearby region. The response matrix files (RMF) and auxiliary response files (ARF) were generated using XISRMFGEN and XISSIMARFGEN, respectively.

Background subtracted light curves obtained from a combination of XIS0, XIS1 and XIS3 detectors are shown in Fig. 2 for all three *Suzaku* observations along with their hardness ratio (HR). Note that while for the lightcurves we have selected a 200 s time bin to resolve flares, HR curves have 2ks time binning chosen to reduce the error.

During both the S1 and S2 observations *Suzaku* observed a number of short flares during which the flux raised up and subsequently dropped down by a factor of 5 on a ks time scale. The S3 observation, done close to the periastron passage, shows a gradual flux rise, with no flares and a constant hardness ratio during the whole observation. The RMS for each light curve is given in Table 2. It is clearly seen that the S3 observation is much smoother than S1 and S2 observations.

Previous studies of the source indicate hardening of the source

<sup>1</sup> <http://heasarc.gsfc.nasa.gov/docs/software/lheasoft/>

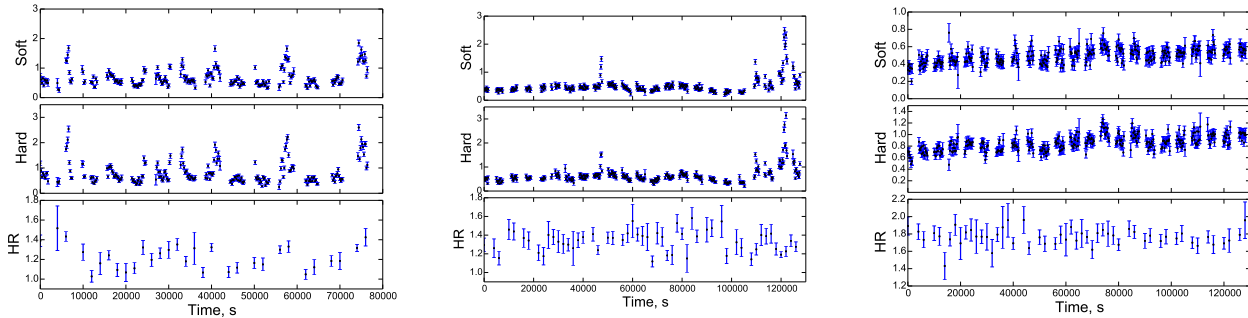


**Figure 2.** The Suzaku lightcurves of LSI +61° 303 in two energy bands (soft = 0.3-2.0 keV, hard = 2.0-10.0 keV) together with their hardness ratio (HR = hard/soft) for all three observations (from left to right, S1, S2, S3). Bin time is 200 s for soft and hard ranges and 2 ks for HR.

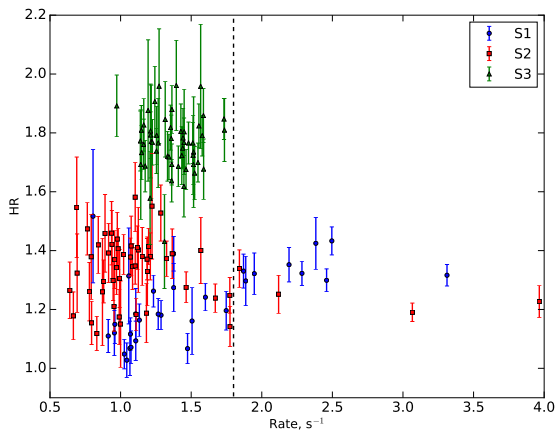


**Figure 3.** HRs versus intensity plot for the all three *Suzaku* observations with a bin time of 2 ks. Count rates correspond to the full energy range 0.3-10.0 keV, and HR is defined as ratio between hard (2.0-10.0 keV) and soft (0.3-2.0 keV) energy bands. Dashed line corresponds to the count rate of 1.8 cts/s used to split S1 and S2 observations, see text for details.

spectrum with the rise of the luminosity, both within the single observation and on a longer time scale (Sidoli et al. 2006; Smith et al. 2009). As shown in Figure 3 we clearly see this dependence in the case of the S1 observation, while in the S2 observation we don't see any hint of spectral hardening during the flares. There were no flares during the S3 observation, but in general it turned out to be much harder than the S1 and S2 observations.

In spectral analysis we have used data only from the front-illuminated CCDs (XIS-0 and XIS-3), which have a larger effective area at high energies, and have almost identical properties, so that it is possible to co-add the data to improve photon statistics. For spectral fitting we used a single power law model with photoelectric absorption (phabs\*powerlaw XSPEC model). This model provides a good fit for all three *Suzaku* observations, see Table 2. Absorption column densities and photon indexes for S1 and S2 are consistent with the previous results of *XMM-Newton* and *Chandra* observations (Sidoli et al. 2006; Albert et al. 2008; Anderhub et al. 2009). For the S3 case (near the periastron), we got a higher value of column density and a lower value for the index. This value of the column density is in agreement with the results obtained by *Chandra* in spring 2006 (Paredes et al. 2007). The spectral slope varies

from 1.6 near periastron to 1.8 – 1.9 near apastron, while column density changes from 0.6 to 0.5.

To compare the spectral shape of the source in and out of the flare we split S1 observation into two parts with total count rates below (S1a) and above (S1b) 1.8 cts/s. Spectral characteristics of S1a and S1b turned out to be quite different indeed, see Table 2 and upper panel of Figure 4. A similar split for the S2 observation (below and above 1.8 cts/s) doesn't show notable change of the spectral index, but instead shows a variation of the column density at a  $1\sigma$  level, see Table 2 and bottom panel of Figure 4.

For the HXD/PIN data, we have used standard event re-processing and screening criteria. The tuned background files were chosen to determine the HXD/PIN non-X-ray background. To extract the source spectrum of LSI +61° 303 we used the `hxdpinxbpi` tool. For the S3 observation HXD/PIN, data (corrected using the standard cross calibration factor of 1.15) lies on the continuation of the power law model used to describe S3 XIS data, see Figure 5. For S1 and S2 observations, however, HXD/PIN points lie well above the model derived from XIS data (cross calibration factor 1.74 for S1 and 2.63 for S2 are needed for a plausible fit). It turned out that during the S1 and S2 observations the temperature of HXD was too high, which resulted in a very high instrumental background leading to telemetry saturation and dead-time of about 50% (typically the dead-time is  $< 10\%$ ). In addition to that during that week there was almost no earth occultation data. Such a situation is not well treated in the current background generation, so that the background was underestimated, leading to extremely high values of the calibration factor.

## 2.2 XMM-Newton observations

The *XMM-Newton* Observatory consists of three X-ray telescopes. Two of these telescopes use MOS CCDs (den Herder et al. 2001) and one uses a PN CCD (Strüder et al. 2001). *XMM-Newton* observed LSI +61° 303 13 times during the last decade (see Tab. 3 for details). These data were already presented in Chernyakova, Neronov & Walter (2006); Sidoli et al. (2006); Anderhub et al. (2009). Here we reanalyzed them using the latest *XMM-Newton* Science Analysis Software v.14.0.0 (SAS). Known hot pixels and electronic noise were removed, and data were cleaned from the influence of the soft proton flares. In our analysis, we have used only PN data to extract all the products. The source spectra were extracted from a circular area of 36 arc seconds radius, and the background spectra were obtained from a nearby, source free region of the same radius. Spectra were rebinned to have at least 30

**Table 2.** *Suzaku* results of spectral fitting with absorbed power law model. In lines marked with (+PIN) we give the result of simultaneous fitting of XIS and PIN data. Value of  $N_H$  is given in  $10^{22} \text{ cm}^{-2}$ , and values of absorbed and unabsorbed fluxes are given in  $10^{-11} \text{ erg cm}^{-2} \text{ s}^{-1}$ . For the S3 observation the PIN calibration factor is found to be  $1.15 \pm 0.11$ , as expected from the standard calibration, while for S1 and S2 observations the fitted values turned out to be too high,  $1.74 \pm 0.20$  and  $2.63 \pm 0.23$ . See text for more details.

Ref	$N_H$	$\Gamma$	$\text{Flux}_{1-10\text{keV}}^{\text{abs}}$	$\text{Flux}_{1-10\text{keV}}$	$\chi^2_{\text{red}}(\text{d.o.f.})$	$\text{RMS}_{1\text{ks}}$
S1	$0.50 \pm 0.01$	$1.86 \pm 0.01$	$1.17 \pm 0.01$	$1.38 \pm 0.01$	0.98 (375)	$0.66 \pm 0.07$
S1(+PIN)	$0.49 \pm 0.01$	$1.86 \pm 0.01$	$1.18 \pm 0.01$	$1.38 \pm 0.01$	0.98 (381)	
S1a	$0.47 \pm 0.03$	$1.97 \pm 0.04$	$0.87 \pm 0.02$	$1.09 \pm 0.02$	1.13 (484)	
S1b	$0.52 \pm 0.02$	$1.88 \pm 0.03$	$2.03 \pm 0.02$	$2.54 \pm 0.02$	1.06 (553)	
S2	$0.50 \pm 0.01$	$1.80 \pm 0.02$	$0.92 \pm 0.01$	$1.08 \pm 0.01$	0.98 (437)	$0.57 \pm 0.08$
S2(+PIN)	$0.49 \pm 0.01$	$1.80 \pm 0.01$	$0.92 \pm 0.01$	$1.08 \pm 0.01$	0.98 (444)	
S2a	$0.53 \pm 0.02$	$1.96 \pm 0.03$	$0.98 \pm 0.01$	$1.19 \pm 0.01$	0.99 (471)	
S2b	$0.49 \pm 0.01$	$1.96 \pm 0.02$	$1.55 \pm 0.01$	$1.88 \pm 0.01$	0.98 (400)	
S3	$0.62 \pm 0.01$	$1.63 \pm 0.01$	$1.21 \pm 0.01$	$1.43 \pm 0.01$	1.04 (559)	$0.17 \pm 0.02$
S3(+PIN)	$0.62 \pm 0.01$	$1.62 \pm 0.01$	$1.21 \pm 0.01$	$1.43 \pm 0.01$	1.04 (575)	

**Table 3.** The log of XMM-Newton observations

Obs. date	ObsID	Ref	MJD	$\phi$	$\Phi$	Exp.time ks	$\text{RMS}_{1\text{ks}}$
05-02-2002	0112430101	X1	52310.072	0.552	0.3652	6.40	$0.13 \pm 0.02$
10-02-2002	0112430102	X2	52315.461	0.756	0.3684	6.40	$0.65 \pm 0.01$
17-02-2002	0112430103	X3	52322.179	0.009	0.3724	6.40	$0.39 \pm 0.01$
21-02-2002	0112430201	X4	52326.639	0.178	0.3751	7.49	$0.22 \pm 0.01$
16-09-2002	0112430401	X5	52533.099	0.970	0.4990	6.46	$0.10 \pm 0.02$
27-01-2005	0207260101	X6	53397.736	0.602	0.0176	50.41	$0.60 \pm 0.01$
04-09-2007	0505980801	X7	54347.075	0.432	0.5871	17.41	$0.28 \pm 0.01$
06-09-2007	0505980901	X8	54349.063	0.507	0.5883	13.41	$0.18 \pm 0.01$
07-09-2007	0505981001	X9	54350.092	0.546	0.5890	18.55	$0.25 \pm 0.01$
08-09-2007	0505981101	X10	54351.060	0.582	0.5895	17.41	$0.33 \pm 0.01$
09-09-2007	0505981201	X11	54352.060	0.620	0.5901	15.01	$0.14 \pm 0.01$
10-09-2007	0505981301	X12	54353.058	0.658	0.5907	16.87	$0.09 \pm 0.01$
11-09-2007	0505981401	X13	54354.060	0.703	0.5913	14.51	$0.27 \pm 0.01$

counts per bin. The response matrix files (RMFs) and auxiliary response files (ARFs) were extracted using RMFGEN and ARFGEN tools, respectively. A single power law model with photoelectric absorption (phabs\*powerlaw XSPEC model) provides a good fit for all *XMM-Newton* observations, see Table 4. It turned out that both spectral index and hydrogen column density varies along the orbit, as is illustrated on the left panel of Figure 7, where we show  $3\sigma$  contour plots. It is clearly seen that for e.g. X5 and X7 observations both slope and column density are different at more than  $3\sigma$  confidence level. During the longest *XMM-Newton* observation, X6, Sidoli et al. (2006) has observed a sharp softening of the source spectrum in the middle of the observation. The dependence of the hardness ratio on the source count rate is shown in Figure 6. In our spectral analysis, similar to S1 and S2 *Suzaku* observations, we split X6 into X6a, with count rate in 0.3 – 12 keV below 1.1 cts/s and X6b with the count rate above 1.1 cts/s. Hardening of the source spectrum with the rise of the source flux is clearly seen (see Table 4 and right panel of Figure 7).

### 2.3 Chandra observations

LSI +61° 303 has been observed by the *Chandra* X-ray observatory 3 times to date (see Table 5). These data were already presented by Paredes et al. (2007); Albert et al. (2008); Rea et al. (2010). For consistency we reanalyze these data with the latest version of software available, CIAO v.4.3 software package and CalDB v.4.3.0.

**Table 4.** Best fit results of the spectral analysis for *XMM-Newton* observations of LSI +61° 303. The flux values are in units of  $10^{-11} \text{ erg/cm}^2/\text{s}$ , while absorption is in units of  $10^{22} \text{ cm}^{-2}$ .

Ref	$N_H$	$\Gamma$	$\text{Flux}_{1-10\text{keV}}^{\text{abs}}$	$\text{Flux}_{1-10\text{keV}}$	$\chi^2_{\text{red}}(\text{d.o.f.})$
X1	$0.47 \pm 0.01$	$1.53 \pm 0.02$	$1.59 \pm 0.02$	$1.84 \pm 0.01$	1.07 (253)
X2	$0.49 \pm 0.02$	$1.49 \pm 0.03$	$1.47 \pm 0.02$	$1.70 \pm 0.02$	1.07 (223)
X3	$0.57 \pm 0.04$	$1.83 \pm 0.07$	$0.76 \pm 0.03$	$0.93 \pm 0.02$	0.98 (95)
X4	$0.43 \pm 0.05$	$1.52 \pm 0.08$	$0.52 \pm 0.02$	$0.62 \pm 0.03$	1.01 (87)
X5	$0.57 \pm 0.02$	$1.57 \pm 0.03$	$1.48 \pm 0.04$	$1.72 \pm 0.02$	0.93 (251)
X6	$0.45 \pm 0.01$	$1.58 \pm 0.01$	$0.98 \pm 0.01$	$1.11 \pm 0.01$	1.14 (1074)
X6a	$0.44 \pm 0.01$	$1.73 \pm 0.02$	$0.50 \pm 0.01$	$0.57 \pm 0.01$	1.05 (223)
X6b	$0.50 \pm 0.01$	$1.61 \pm 0.02$	$1.44 \pm 0.02$	$1.67 \pm 0.01$	1.12 (289)
X7	$0.45 \pm 0.01$	$1.82 \pm 0.02$	$0.83 \pm 0.09$	$0.95 \pm 0.01$	1.07 (357)
X8	$0.44 \pm 0.01$	$1.61 \pm 0.02$	$0.86 \pm 0.01$	$0.96 \pm 0.01$	1.09 (348)
X9	$0.46 \pm 0.01$	$1.60 \pm 0.02$	$0.91 \pm 0.01$	$1.03 \pm 0.01$	1.29 (505)
X10	$0.45 \pm 0.01$	$1.62 \pm 0.02$	$0.92 \pm 0.01$	$1.02 \pm 0.01$	0.97 (500)
X11	$0.48 \pm 0.01$	$1.51 \pm 0.01$	$1.62 \pm 0.02$	$1.80 \pm 0.01$	1.15 (634)
X12	$0.47 \pm 0.01$	$1.53 \pm 0.02$	$1.31 \pm 0.01$	$1.44 \pm 0.01$	1.08 (513)
X13	$0.46 \pm 0.01$	$1.58 \pm 0.02$	$0.88 \pm 0.01$	$0.98 \pm 0.01$	1.10 (376)

To extract source and background spectra with RMF and ARF we used the *specextract* tool. The source spectra were extracted from a circular area around the source with a 3 arc seconds radius, while the background spectra were made from a nearby region with no source and with the same 3 arc second radius. The source spectra

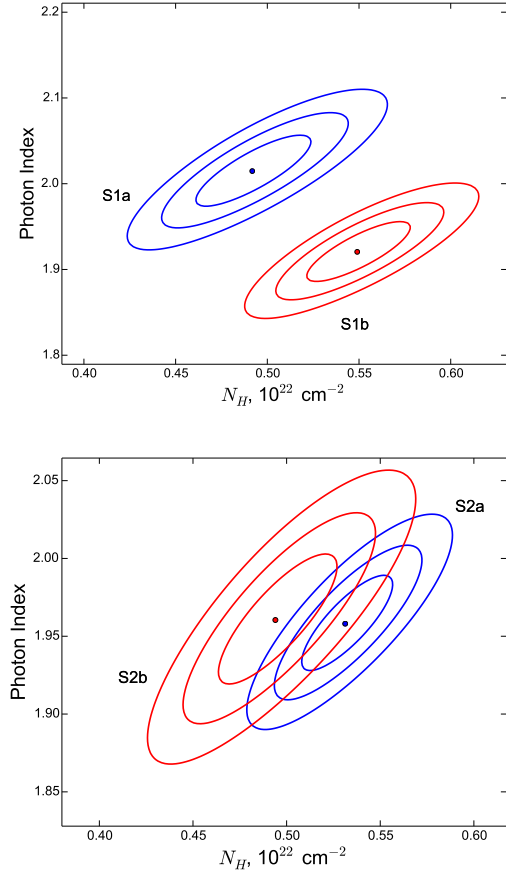


**Figure 4.** 1, 2 and 3 $\sigma$  confidence contour plots of the column density  $N_H$  versus photon spectral index  $\Gamma$  for a power-law fit to S1a and S1b observations (top panel) and S2a and S2b (bottom panel).

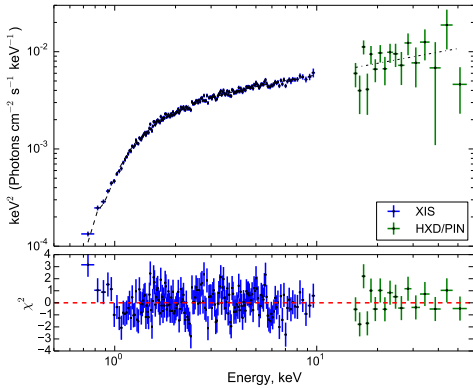


**Figure 5.** *Suzaku* spectrum of S3 observation fitted with absorbed power law model.

were grouped to have at least 30 counts per bin. The fitting of spectra was performed in XSPEC environment with `phabs*powerlaw` model. Following the work of Paredes et al. (2007) we have also added the pileup model to the absorbed power law for the first *Chandra* observation C1. For this observation we fixed the event pileup fraction parameter  $f$  to 0.95, and the grade migration pa-

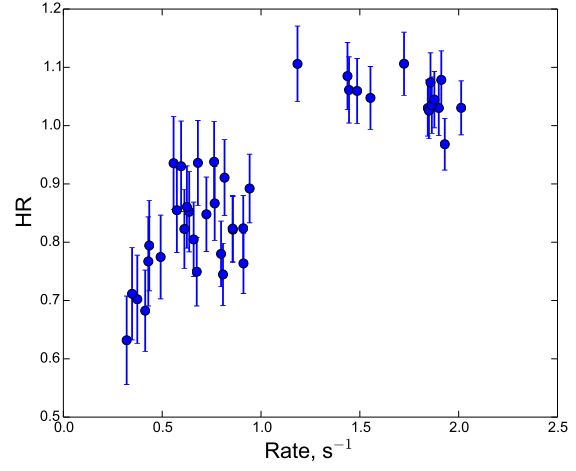


**Figure 6.** The dependence of HR (ratio of count rate in the 2 – 12 keV energy range to count rate in the 0.3 – 2 keV energy range) on the count rate in the full energy band (0.3-12.0 keV) as observed by *XMM-Newton* during X6 PN observation. Time binning is 1 ks.

**Table 5.** The log of *Chandra* data of LSI +61° 303

Obs. date	ObsID	Ref	MJD	Instr.	Exp.time	$\phi$	$\Phi$
			d		ks		
07-04-2006	6585	C1	53832.922	ACIS-I	49.73	0.027	0.2787
25-10-2006	8273	C2	54033.925	ACIS-I	20.03	0.613	0.3993
14-11-2008	10052	C3	54784.460	ACIS-S	95.67	0.940	0.8495

rameter was found to be  $\alpha = 0.33 \pm 0.09$ . The results of the fitting are shown in Table 6.

## 2.4 *Swift* observations

Observations performed by the *Swift* observatory during the last few years give a unique chance to monitor the behaviour of LSI +61° 303 on a range of time scales. In this work we used data spanning over more than 4 years between 2010 and 2014. The data reduction was done using tools and packages available in FT00LS/HEASOFT 6.16. LSI +61° 303 was observed both in Photon Counting (PC) and Windowed Timing (WT) modes. After initial cleaning of events using `xrtpipeline` with standard parameters we selected 164 observations. Further analysis was performed following Evans et al. (2009). In particular, in the PC mode the source extraction region was a circle with radius from 5 to 30 pixels depending on the count rate (Evans et al. 2009); in the WT mode the radius of the source extraction region was 25 pixels. The background was collected over the annular region with an inner (outer)

**Table 6.** The best fit parameters of *Chandra* data of LSI +61° 303. Value of  $N_H$  is given in  $10^{22} \text{ cm}^{-2}$ , and values of absorbed and unabsorbed fluxes are given in  $10^{-11} \text{ erg/cm}^2/\text{s}$

Ref	$N_H$	$\Gamma$	$F_{1-10\text{keV}}^{\text{abs}}$	$F_{1-10\text{keV}}$	$\chi^2/\text{dof}$	$\text{RMS}_{1\text{ks}}$
C1	$0.65 \pm 0.045$	$1.30 \pm 0.08$	$0.50 \pm 0.01$	$0.60 \pm 0.01$	1.19/293	$0.36 \pm 0.01$
C2	$0.56 \pm 0.02$	$1.55 \pm 0.02$	$2.32 \pm 0.04$	$2.66 \pm 0.02$	1.03/329	$0.52 \pm 0.01$
C3	$0.59 \pm 0.01$	$1.78 \pm 0.01$	$0.82 \pm 0.01$	$0.98 \pm 0.01$	1.09/460	$0.19 \pm 0.01$

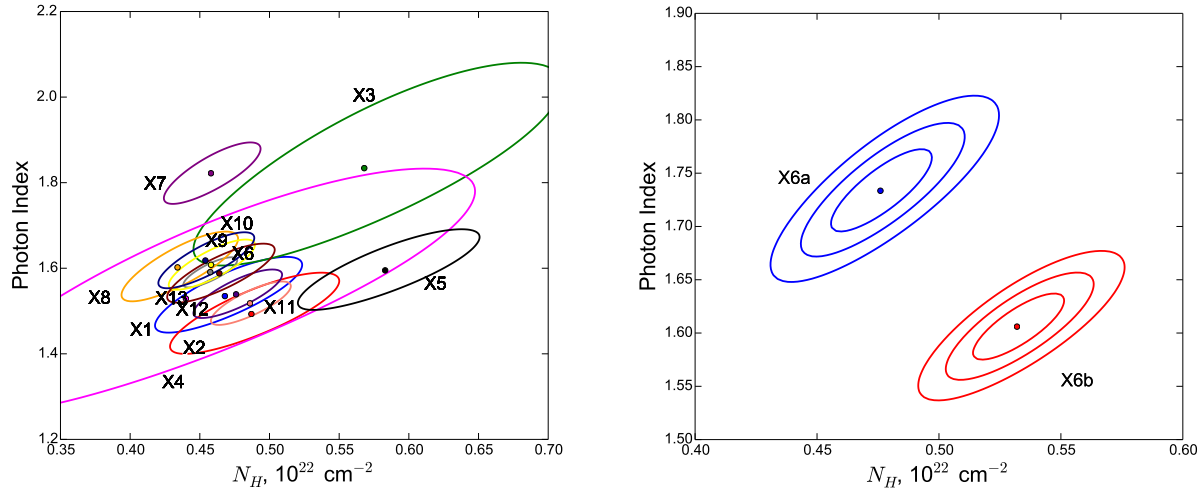


**Figure 7.** Contour plots of the column density  $N_H$  versus photon spectral index  $\Gamma$  for a power-law fit to all *XMM-Newton* observations (left panel, only  $3\sigma$  contours are shown) and X6a and X6b (right panel, 1, 2, and  $3\sigma$  contours are shown).

radius of 60 (110) pixels in both observational modes. The count rate from the source was too low to pile up the detector in all observations.

Since the statistics of the data is poor, the spectra were grouped to have at least 1 count bin<sup>-1</sup> using the *FTOOLS* *grppha* tool. The spectral analysis was performed in *XSPEC* environment and the spectra were fitted at 0.5 – 10.0 keV energy band. The errors reported in this work are purely statistical and correspond to a  $1\sigma$  confidence level. For most of the observations the statistic was too poor to draw any conclusions from a single observation. Thus we selected observations from similar orbital and superorbital phases and fitted them together. The results are given in Table 7 and Figure 8, which show the 1.0 - 10.0 keV X-ray flux, column density and photon index from the source as a function of the orbital and superorbital phases. Note that each point in this figure is a combination of several closely spaced observations. Green error bars correspond to the  $1\sigma$  errors of the spectral fit, while blue error bars were calculated taking into account the spread of spectral parameters of the individual observations (following the equation for RMS given in section 2.1). These latter error bars represent the potential variability of the source in each of the orbital phase bins; however, they should be treated with caution given the poor statistics of the single *Swift* measurements. One can see that in agreement with previous findings (Chernyakova et al. 2012; Li et al. 2012) the flux is maximal during the 0.2-0.4 superorbital phase, with a peak becoming wider and moving from orbital phase  $\phi \sim 0.4$  at superorbital phase  $\Phi = 0 - 0.2$  to orbital phase  $\phi \sim 0.8$  at superorbital phase  $\Phi = 0.4 - 0.6$ . During the superorbital phases  $\Phi = 0.6 - 0$  the peak disappears, or become too narrow to be detected with such wide bins. On the contrary, the values of column density and photon index are consistent with a constant value, the same for all orbital and superorbital phases (the averaged value of column density is equal to  $\langle N_H \rangle = 0.55 \pm 0.01$ , RMS=0.24; the averaged value of spectral index is equal to  $\langle \Gamma \rangle = 1.54 \pm 0.02$ , RMS=0.32). The evolution of the source X-ray flux with the orbital phase shows X-ray emission along all the phases, although with a difference of a factor 3 in the flux level between two states, with a “high” state preferentially found in the phase range 0.4-1.0.

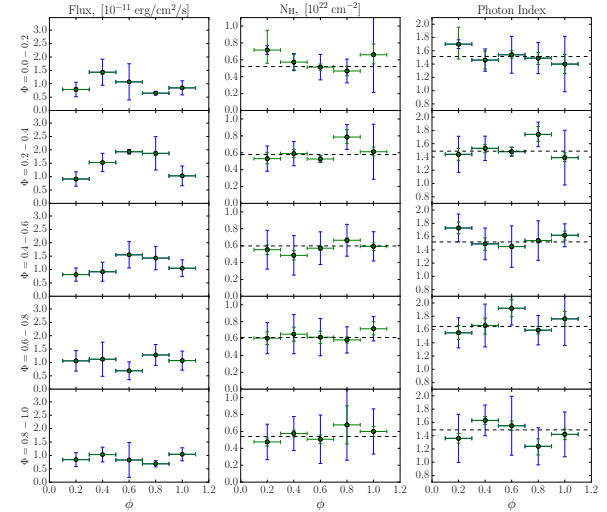


**Figure 8.** Dependence of flux, column density and spectral index on the orbital phase at different superorbital phases as measured by *Swift*.

### 3 VARIABILITY ON DIFFERENT TIME SCALES.

#### 3.1 Minimal variability time scale

In addition to well-established orbital and superorbital modulations, the X-ray flux of the LSI +61° 303 binary system experiences much faster variability, signatures of which were found in almost all observational periods, described above. The detection of this variability allows us to address the physics of the X-ray emission region in the system through the measurement of the characteristic time scales, associated with it, as well as the overall shape of its power spectrum density (PSD).

In order to assess the character and time scale of this variability, we analysed all available *Suzaku*, *Chandra* and *XMM-Newton*

<sup>1</sup> <https://heasarc.gsfc.nasa.gov/xanadu/xspec/manual/XSappendixStatistics.html>,  
<http://xc.harvard.edu/sherpa/ahelp/cstat.html>



**Table 7.** Best fit results of the spectral analysis for *Swift* observations of LSI +61° 303 sampled along different orbital and superorbital phases. The flux values are in units of  $10^{-11}$  erg/cm<sup>2</sup>/s, while absorption in units of  $10^{22}$  cm<sup>-2</sup>. “C-stat” represents the value of the Cash statistic<sup>1</sup>, estimated by XSpec.

$\phi$	$\Phi$	$F_{1-10\text{keV}}$	$N_H$	$\Gamma$	C - stat	$\chi^2/\text{(d.o.f)}$
0.9-1.1	0.8-1.0	1.04±0.03	0.60±0.06	1.42±0.08	430.71	1.22/484
0.7-0.9	0.8-1.0	0.68±0.01	0.68±0.22	1.24±0.13	325.39	1.00/408
0.5-0.7	0.8-1.0	0.83±0.02	0.51±0.05	1.55±0.07	442.72	1.25/508
0.3-0.5	0.8-1.0	1.03±0.02	0.58±0.04	1.63±0.06	447.92	1.04/570
0.1-0.3	0.8-1.0	0.84±0.03	0.48±0.05	1.36±0.07	456.42	1.28/493
0.9-1.1	0.6-0.8	1.07±0.04	0.72±0.08	1.76±0.11	278.34	0.92/379
0.7-0.9	0.6-0.8	1.28±0.03	0.58±0.04	1.59±0.06	568.44	1.35/598
0.5-0.7	0.6-0.8	0.69±0.03	0.62±0.07	1.92±0.13	259.08	1.06/324
0.3-0.5	0.6-0.8	1.12±0.05	0.65±0.08	1.66±0.13	303.18	1.14/356
0.1-0.3	0.6-0.8	1.06±0.04	0.60±0.07	1.55±0.11	307.78	0.96/411
0.9-1.1	0.4-0.6	1.05±0.02	0.59±0.05	1.62±0.07	495.65	1.18/559
0.7-0.9	0.4-0.6	1.43±0.02	0.66±0.03	1.54±0.04	779.45	1.40/723
0.5-0.7	0.4-0.6	1.55±0.02	0.57±0.03	1.45±0.03	750.02	1.32/747
0.3-0.5	0.4-0.6	0.92±0.04	0.48±0.05	1.49±0.10	370.82	1.38/408
0.1-0.3	0.4-0.6	0.81±0.03	0.55±0.06	1.73±0.09	363.66	1.28/434
0.9-1.1	0.2-0.4	1.03±0.02	0.61±0.06	1.39±0.07	585.15	1.36/591
0.7-0.9	0.2-0.4	1.87±0.08	0.79±0.08	1.78±0.12	301.17	1.02/378
0.5-0.7	0.2-0.4	1.93±0.05	0.53±0.04	1.48±0.06	497.10	1.12/577
0.3-0.5	0.2-0.4	1.53±0.04	0.59±0.05	1.53±0.06	524.21	1.33/562
0.1-0.3	0.2-0.4	0.91±0.04	0.53±0.07	1.44±0.09	361.12	1.19/434
0.9-1.1	0.0-0.2	0.84±0.05	0.66±0.11	1.40±0.14	203.29	0.97/250
0.7-0.9	0.0-0.2	0.65±0.02	0.47±0.06	1.49±0.10	350.87	1.13/413
0.5-0.7	0.0-0.2	1.07±0.02	0.51±0.04	1.54±0.06	584.30	1.32/599
0.3-0.5	0.0-0.2	1.43±0.07	0.57±0.09	1.36±0.14	244.08	1.05/317
0.1-0.3	0.0-0.2	0.79±0.06	0.72±0.23	1.70±0.26	135.98	0.93/180

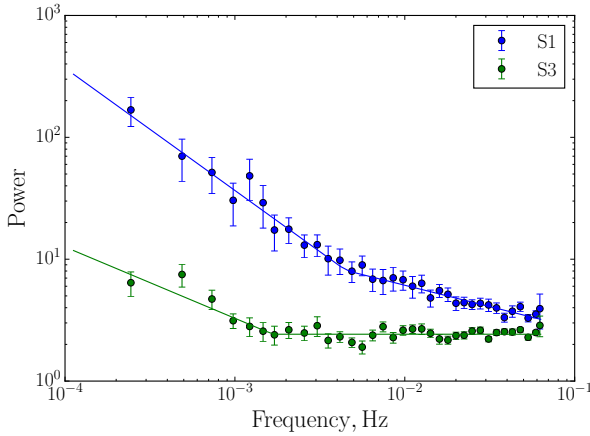


**Figure 9.** The FFT power spectra of the S1 and S3 observations of LSI +61° 303. The solid lines represent the corresponding fits with the broken power law. Time bin of the light curves used is 8 s.

observations; the *Swift* observations turned out to be short to investigate ~ks variability, detected here with other instruments, and thus were not included to the analysis. We also additionally checked, that none of the single *Swift* observations shows evidences for the flux variability, being inconsistent with a constant at a more than  $3\sigma$  significance level.

For each of the analysed observations we computed the power spectrum with the help of *powspec* tool from the *FTOOLS* pack-

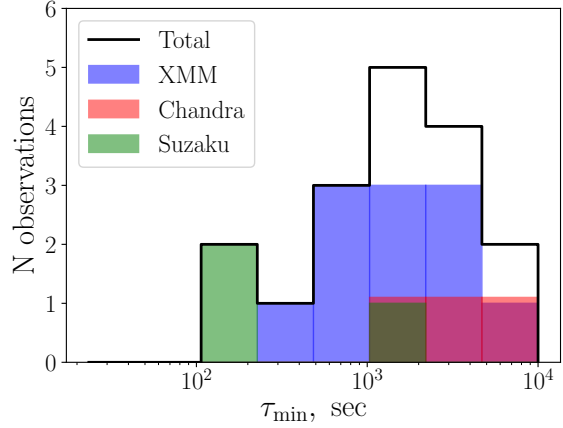


**Figure 10.** Distribution of the minimal variability time scales, derived with the Structure Function analysis (see Sect. 3.1 for details). Chandra points were artificially raised by 10% to improve the visual perception.

age<sup>2</sup>. The examples of the derived power spectra – for S1 and S3 observations – are shown in Figure 9. For these two data sets the derived spectra exhibit clear breaks in the frequency range  $10^{-3} - 10^{-2}$  Hz. Still, the slope of the S1 PSD (which never becomes flat) and small uncertainties in the S3 PSD suggest that the minimal variability time scale in these data sets can be below ~ 100 s.

However for most of the observations large statistical errors prevent us from determining the break frequency at which the PSD changes its shape. Thus we have to use other means to look for both the minimal and typical variability time scales in the light curves. The minimal variability time scale was searched for by means of the Structure Function (SF) analysis as well as the scanning procedure, described in Chernyakova et al. (2015). The minimal variability time scale  $\tau_{min}$  we defined as the point in SF, where its local power law index does not equal 0 or 2 (SF  $\sim \tau^\alpha$  with  $\alpha = 0$  for white noise and  $\alpha = 2$  for linearly increasing flux, see Vovk & Neronov 2013). The histogram of the derived values of  $\tau_{min}$  is shown in Fig. 10.

The typical value of  $\tau_{min}$ , revealed by the SF analysis, lies in the range ~ 200 – 1000 s (larger values mostly correspond to the observations where no significant variability was detected; for such data sets  $\tau_{min}$  is comparable to the observation duration). Still, a visual inspection of the SF shape suggests that for the C1, X4, X6 and X8 observations the SF does not reach an  $\alpha = 0$  plateau at the lowest time scales and rather continues a power law decline. Though this effect is not significant (i.e. does not reach the  $3\sigma$  threshold), this suggests that for these observations the minimal variability time scale may be shorter than what can be resolved by our analysis - i.e.  $\tau_{min} \lesssim 200$  s. For these observations, we can put an upper limit on the variability amplitude below 200 s at the level of  $\Delta F/F \sim 15 - 30\%$ .

### 3.2 Flux variability along the orbit

Another interesting point is a change in the flux variability scale along the orbit. Figure 11 top shows the fluxes detected by *Swift* in

<sup>2</sup> [https://heasarc.gsfc.nasa.gov/ftools/ftools\\_menu.html](https://heasarc.gsfc.nasa.gov/ftools/ftools_menu.html)

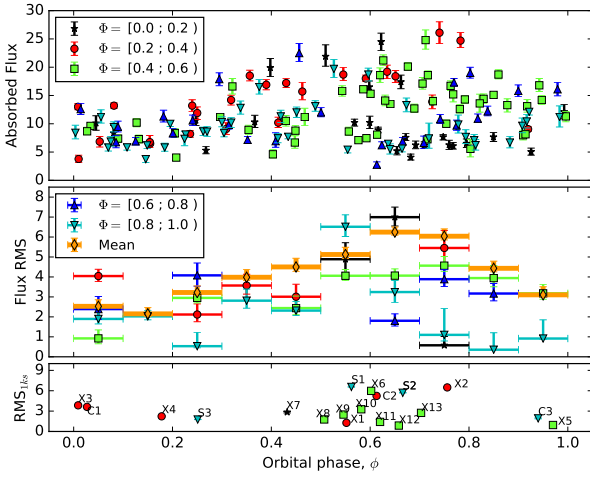


**Figure 11.** *Top panel:* Absorbed flux (1-10 keV, in units  $10^{-12}$  erg/cm<sup>2</sup>/s), measured by *Swift* as a function of orbital phase for the specified superorbital phase ranges. *Middle panel:* RMS of the shown on the top panel fluxes for the specified superorbital phase ranges. Orange diamond points stand for the RMS at given orbital phase averaged over all superorbital phases. *Bottom panel:* RMS<sub>1ks</sub> for the individual observations of XMM-Newton, Chandra, Suzaku, see Tables 2,3,6. In all panels the colour scheme corresponds to the superorbital phase ranges according to the legend.

individual observations as a function of an orbital phase. Different colours correspond to different superorbital phases.

As it was proposed in Chernyakova et al. (2012) RXTE observations indicate the disruption of the Be-star disk at superorbital phase  $\sim 0.6$ . After this event the size of the disk is gradually increasing up to its next disruption. The similar behaviour is seen in *Swift* data, see middle panel of Fig. 11. The maximal flux variability can be naturally expected as the compact object intersects the clumpy outer regions of the disk. The shift of the RMS maximum from  $\phi = 0.55$  at superorbital phase  $\Phi = 0.8 - 1$  to  $\phi = 0.65$  at  $\Phi = 0.0 - 0.2$  and  $\phi = 0.75$  at  $\Phi = 0.2 - 0.4$  in this case can be interpreted as a gradual increase of the disk size at superorbital time scales. At the same time green and blue points do not show clear orbital variation. Such a behaviour can be expected if the compact object spend the whole orbit inside the dense homogeneous regions of the near-to-maximum size disk. The evolution of the averaged over superorbital phase RMS (see orange points) also indicates that close to periastron the compact object is embedded into the smooth dense region of the Be star disk (most stable with respect to superorbital changes), while closer to the apastron the compact object moves in clumpy outskirts of the disk.

The lower panel shows the scatter of the flux in individual observations of XMM-Newton/Chandra/Suzaku. The highest RMS values are located around the phase  $\phi = 0.6$  and are accompanied by a large RMS scattering. Similar to the *Swift* data, this can be interpreted as the highest clumps number and the strongest superorbital-scale variations of the disk close to apastron. Further evidence for the clumpy structure of the disk's outskirts can be seen in long XMM-Newton (X6) and Suzaku (S1) observations performed around the phase  $\phi = 0.6$ , where one sees the variability of the column density within a single observation, see Fig. 4, 7.

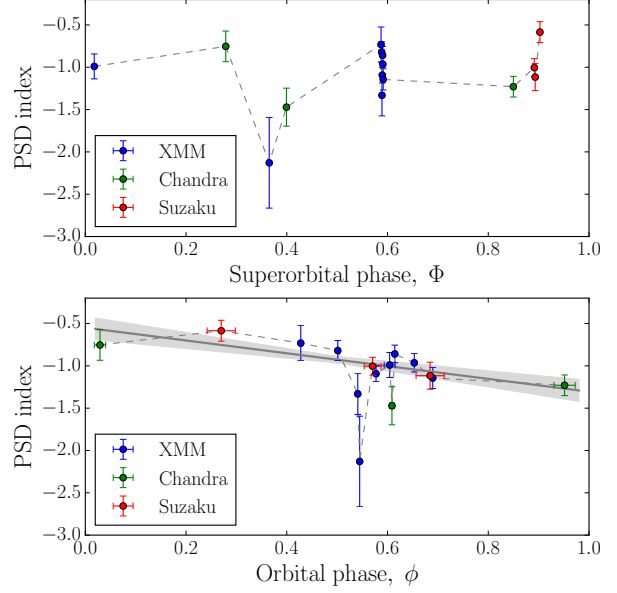


**Figure 12.** *Upper panel:* evolution of the power spectral density index  $\alpha$  of LSI +61° 303 as a function of the superorbital phase. *Lower panel:* the same as a function of the orbital phase. The dashed lines, joining the data points in both panels, are just to guide the eye. The continuous line and the grey shaded region represent the obtained best fit to the linear fit together with its uncertainties.

### 3.3 Variability on longer time scales

The long time scale variability of LSI +61° 303 has been well studied at different energy ranges (e.g. Chernyakova et al. (2012); Ackermann et al. (2013)). In addition to the previously known flux modulation with the orbital/superorbital phase, we notice here, that the short time scale variability pattern also varies along the orbit. This pattern can be quantified in terms of the power law index (slope)  $\Gamma$  of the Fourier power spectrum density (PSD) for each of the analysed observations.

To obtain the PSD we processed each observation with the *powspec* tool from the HEASoft software package. To account for the presence of the white noise in the measurements we fitted the resulting PSD with the broken power law:

$$P(\nu) = \begin{cases} P_0 * (\nu/\nu_{br})^\alpha, & \nu < \nu_{br} \\ P_0 * (\nu/\nu_{br})^\beta, & \nu \geq \nu_{br} \end{cases} \quad (2)$$

The obtained values of the lower-frequency index  $\alpha$  are summarised in Fig. 12, which shows their dependence on the orbital and superorbital phases.

For some of the data sets the obtained PSD was consistent with the white noise, so no estimate of  $\alpha$  could have been obtained. The corresponding data points are thus not shown in Fig. 12. Also not shown there is the outcome of the *Swift* observations – due to their short durations a reliable estimation of their PSD was not possible. Grouping the *Swift* data in wide orbital phase bins we still find them consistent with a white noise; the resulting uncertainties are, though, too large to result in any inconsistency with the other measurements, displayed in Fig. 12.

This Figure indicates that the PSD slope follows a characteristic pattern and seems to be periodic with the orbital period of the binary. Over the orbit the slope gradually decreases from  $\alpha \approx -0.6$  to  $\alpha \approx -1.2$  and abruptly changes back to the ini-



tial value at phase  $\phi \approx 0$  (see the lower panel of Fig. 12). In order to estimate its significance we have performed the linear fit ( $y = k(x - 0.5) + b$ ) to the obtained data points, which resulted in  $\chi^2/d.o.f = 20.2/13$  for  $k = -0.8 \pm 0.2$  and  $b = -0.93 \pm 0.04$ , compared to  $\chi^2/d.o.f = 36.0/14$  for the angular coefficient fixed at  $k = 0$ . This corresponds to a  $\approx 4\sigma$  significance of the detected trend. The obtained best-fit line together with its uncertainties is shown in grey in the lower panel of Fig. 12.

The hardest slope  $\alpha \approx -0.6$  is found close to the periastron at phase  $\phi = 0.275$ . As the PSD slope characterises the relative power of the long and short time scale variability, this behaviour indicates the increasing fraction of the short time scale variations as the compact object moves closer the Be star. The minimal contribution of the short variability is found at  $\phi \approx 0.55$ , approximately 5 days before the apastron.

It is reasonable to assume that the observed variability of the X-ray flux originates from inhomogeneities in the Be companion wind flow, resulting in a varying supply of material to the compact object. The measured PSD slope in this case simply reflects the short- (high frequencies) and long- (low frequencies) scale structure of the wind, encountered by the compact object along its orbit. Given the frequency range  $\nu \sim 10^{-4} - 10^{-2}$  Hz of our power density spectra and the orbital velocity of the compact object, these measurements are sensitive to wind inhomogeneities of  $l = v/\nu \sim 10^4 - 10^6$  km in size (assuming the average velocity of the compact object  $v \approx 100$  km/s).

This assumption provides a reasonable explanation of the observed behaviour of the PSD slope. As the compact object moves towards the Be star, it encounters progressively more structured (on the scales  $< 10^6$  km) regions of the Be decretion wind flow. The first passage of the compact object through the disk at  $\phi \sim 0$  put it in a very inhomogeneous environment, as revealed by the sudden increase of the PSD slope to  $\alpha \approx -0.7$ . Further advance of the compact object brings it to an even more inhomogeneous region, potentially resulting from the disruption of the decretion of the disk by the compact objects's gravity. Gradual growth of  $\alpha$  (and the fraction of the short time scale variability) continues until the periastron, after which  $\alpha$  starts to gradually decrease as the compact object moves away from the Be star to the less structured, distant regions of the orbit.

The absence of a clear correlation between the PSD  $\alpha$  and the superorbital phase suggests that this picture does not qualitatively change with the gradual build-up of the Be disk. However, the sampling of the available observations is too sparse to make any firm conclusions on this matter.

#### 4 DISCUSSION

The short and long time scale variability of LSI +61° 303 reported here, provides important insights to the physical picture of the system, outlined in Chernyakova et al. (2012). The gradual build up and the subsequent destruction of the Be star disk constantly changes the conditions of medium, travelled through by the compact object. This all results in a different level of the disk fragmentation, which can be traced with the variability of the observed X-ray flux.

The presented observations demonstrate that both spectral and flux variability in LSI +61° 303 happen already on the hour time scales. It is reasonable to assume, that this variability is caused not by the compact object itself, but rather by it probing the stellar wind

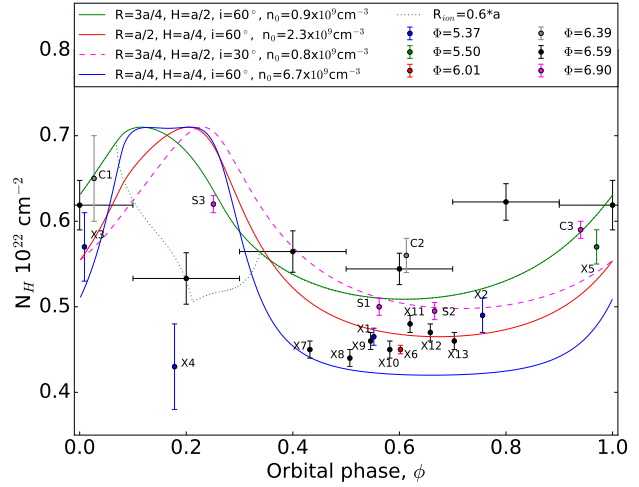


**Figure 13.**  $N_H$  orbital evolution in LSI +61° 303 as observed by *Suzaku* (S1, S2 and S3), *XMM-Newton* (X1 - X13), *Chandra* (C1, C2, C3) and *Swift* (black points with big horizontal error bars). Lines illustrates the  $N_H$  behaviour predicted by the model described in the text for different sizes of the disk. Dotted green line illustrates the possible effect of the disk ionisation close to the star. The radius  $R$  and the height scale of the disk  $H$  are given in units of the major semiaxis  $a$ .

regions of different structure (blob size and density) in the course of its movement around the star.

This assumption is supported by the orbital and superorbital modulation of variability, illustrated in Fig. 11 in terms of the flux RMS. Indeed, in most of the MHD models of the Be star decretion disks their interior regions remain relatively homogeneous due to higher density, whereas the outskirts present highly structured, clumpy structure (Runacres & Owocki 2002). The orbital modulation of the flux RMS agrees with this picture, being lowest close to the epoch of periastron and gradually increasing towards the most distant part of the compact object's orbit at phase  $\sim 0.7$ .

Further support to this picture is provided by the PDS variations, shown in Fig. 12. Indeed, the gradual softening of the PDS index after the periastron passage suggests the small-scale blobs become rare – as a result of their growth due to the internal pressure and the overall rarefaction of the disc.

In addition to this qualitative picture, the available data allow to obtain some quantitative information about the disk regions, interacting with the compact object. Though their structure can be assessed (at least to a certain extent) from the variability, the overall density of the disk can be obtained from the absorption signatures in the detected X-ray flux.

In Figure 13 we summarise the measurements of the  $N_H$  column density, stemming from the analysis described in Section 2. The value of  $N_H$  is clearly non-constant along the orbit with a  $\chi^2 = 458.6$  for 18 degrees of freedom, suggesting the variability at the  $19.6\sigma$  level. Within the simplest model, the observed value of  $N_H$  at each orbital/superorbital phase is given by the integration of the smooth Be star disk density profile along the line of sight to the observer. The presence of clumps in the wind and/or the regions with highly or partially ionised hydrogen can, however, significantly modify the predictions for the observed  $N_H$  values.

We assume that the Be star disk consists of non-ionized hydrogen and has an exponential density profile characteristic of isothermal atmosphere:

$$n_D = n_0 \exp(-r/R - |z|/H)$$

In such a simple case one can expect to see a maximum of the column density when the compact object crosses the periastron if an observer looks at the system in the direction perpendicular to the disk, or when the compact object passes the superior conjunction, if an observer is located in the orbital plane. In Figure 13 we show the  $N_H$  orbital evolution for different parameters of the disk (the contribution of the galactic  $N_H$  was set to  $N_{Hgal} = 0.42 \times 10^{22} \text{ cm}^{-2}$  for the best match to the data)<sup>3</sup>. In this plot the solid lines correspond to the case of inclination  $i = 60^\circ$ , and the dashed one to the case of  $i = 30^\circ$ . As expected the orbital position of the maximum column density shifts toward the phase of periastron,  $\phi = 0.275$  with the decrease of the inclination of the observer. In all cases, the derived number density of the disk is  $n_0 \sim 10^{-9} \text{ cm}^{-3}$  – close that typically found for other Be stars (Rivinius, Carciofi & Martayan 2013).

The small number of the available observations around the periastron does not allow to investigate the variations of  $N_H$  in finer phase bins. Nevertheless we note that the nearby points S3 and X4 are marginally inconsistent. To explore this issue we have averaged all the *Swift* data points presented in Table 7 over the superior orbital phases. The resulting profile, shown with black points in Fig. 13, experiences the same drop of the column density at the orbital phase  $\sim 0.2$ . A possible explanation of this behaviour could be an ionisation of the inner disk regions by the UV emission of Be star. To qualitatively test this possibility, we have assumed the fully ionised disk region of a size  $R_{ion}$  does not contribute to the absorption of X-ray flux and repeated the modelling outlined above. The obtained  $N_H$  profile, depicted with the green dotted line in Figure 13, shows the immediate drop of the observed  $N_H$  values around the periastron and its fast recovery afterwards, in concordance with the observed behaviour (the dotted and solid green lines in the figure correspond to the same configuration of the disk but with and without ionisation). Clearly, the available dataset is too limited to move beyond this qualitative picture; still it demonstrates that a dedicated observational campaign of the periastron passage may shed light on the ionisation state of the inner regions of the decretion disk.

At the same time, the observed distribution of  $N_H$  can originate from the constant  $N_H$  level modified by the presence of dense clumps that intersect the line of sight and effectively increase the  $N_H$  on short time scales. From this point of view, the distribution of measured  $N_H$  values<sup>4</sup>, shown in Fig. 14 may help to infer the properties of this clumpy medium.

The obtained distribution is best described with the “gaussian rise, exponential decay” profile, which may indicate the presence of another source of scatter in the data - in addition to the statistical one. This former can originate either from un-accounted for systematic errors in  $N_H$  measurements or from a stochastic variation of the Be star disk density, with the dispersion exceeding the uncertainties of the presented data. In other words, the “gaussian rise, exponential decay” profile corresponds to the presence of the disk clumps with a certain distribution of densities/sizes.

In this case, the exponent decay scale  $N_{H,dec} \approx 0.07 \cdot 10^{22} \text{ cm}^{-2}$  would correspond to the characteristic column density of the clumps. Assuming mean density of the disk to be  $n_0 \sim 10^9 \text{ cm}^{-3}$  (Rivinius, Carciofi & Martayan 2013), this translates into the

<sup>3</sup> We would like to note, that this value is less than the total galactic  $N_H$  value in LSI +61° 303 direction ( $0.7 - 0.9 \cdot 10^{22} \text{ cm}^{-2}$ ) and is in agreement with the value that can be deduced from 3D hydrogen distribution maps used by GALPROP code (Vladimirov et al. 2011).

<sup>4</sup> These data are summarized in Tables 2,4,6. Please note, that the observations S1a, S1b, and S2a, S2b were considered as individual data points

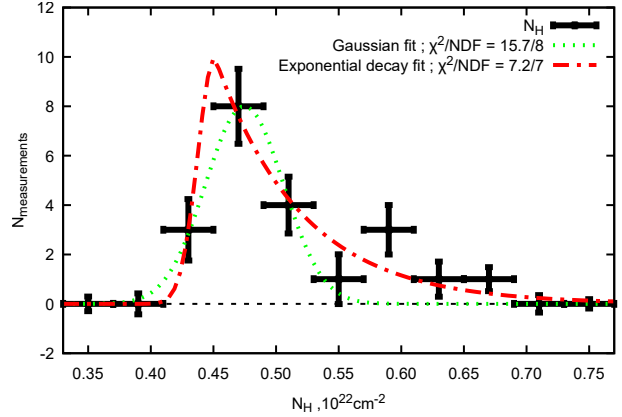


**Figure 14.** The distribution of  $N_H$  column densities for the *XMM-Newton*, *Chandra* and *Suzaku* data shown in Fig. 13. Green dashed and red dot-dashed curves correspond to the fit of the distribution with a single gaussian and “gaussian rise, exponential decay” profiles. The error bars for the distribution were estimated from  $10^4$  random realisations of the original  $N_H$  dataset. In each random realization  $N_H$  values were selected to be gaussian-distributed random variables with the mean and dispersion given by the original distribution.

size of the clumps  $s = N_H/n_0 \sim 7 \cdot 10^{11} \text{ cm}$ , comparable with the radius of the Be star. The obtained value is larger than the spatial scales  $\sim 10^9 - 10^{11} \text{ cm}$ , accessible from the variability detections, described in Sect. 3.3. This suggests that longer,  $\sim 100$  ks continues observations are needed to fully characterise the structure of the disk. In addition to this, an accurate measurement of the disk density profile requires a much denser observational sampling along the orbit at different superior orbital phases, clearly still accessible with the current generation of the X-ray instruments.

#### Acknowledgements

This work was partially supported by the EU COST Action (COST-STSM-MP1304-28864) “NewCompStar”. The authors thank SFI/HEA Irish Centre for High-End Computing (ICHEC) for the provision of computational facilities and support. The work of IuB was partially supported by the Stipendium of the President of Ukraine (2014-2016). DM was supported by the Carl-Zeiss Stiftung through the grant “Hochsensitive Nachweistechnik zur Erforschung des unsichtbaren Universums” to the Kepler Center für Astro- und Teilchenphysik at the University of Tübingen.

#### REFERENCES

- Ackermann M. et al., 2013, *ApJ*, 773, L35
- Albert J. et al., 2008, *ApJ*, 684, 1351
- Anderhub H. et al., 2009, *ApJ*, 706, L27
- Aragona C., McSwain M. V., Grundstrom E. D., Marsh A. N., Roettenbacher R. M., Hessler K. M., Boyajian T. S., Ray P. S., 2009, *ApJ*, 698, 514
- Caliandro G. A., Torres D. F., Rea N., 2012, *MNRAS*, 427, 2251
- Chernyakova M., Neronov A., Molkov S., Malyshev D., Lutovinov A., Pooley G., 2012, *ApJ*, 747, L29
- Chernyakova M. et al., 2015, *MNRAS*, 454, 1358
- Chernyakova M., Neronov A., Walter R., 2006, *MNRAS*, 372, 1585
- den Herder J. W. et al., 2001, *A&A*, 365, L7

- Evans P. A. et al., 2009, MNRAS, 397, 1177  
Gregory P. C., 2002, ApJ, 575, 427  
Jaron F., Massi M., 2014, A&A, 572, A105  
Koyama K. et al., 2007, PASJ, 59, 23  
Li J., Torres D. F., Zhang S., 2014, ApJ, 785, L19  
Li J., Torres D. F., Zhang S., Hadasch D., Rea N., Caliendo G. A., Chen Y., Wang J., 2012, ApJ, 744, L13  
Massi M., Jaron F., 2013, A&A, 554, A105  
Massi M., Jaron F., Hovatta T., 2015, A&A, 575, L9  
Paredes J. M., Ribó M., Bosch-Ramon V., West J. R., Butt Y. M., Torres D. F., Martí J., 2007, ApJ, 664, L39  
Paredes-Fortuny X., Ribó M., Bosch-Ramon V., Casares J., Fors O., Núñez J., 2015, A&A, 575, L6  
Rea N., Torres D. F., van der Klis M., Jonker P. G., Méndez M., Sierpowska-Bartosik A., 2010, MNRAS, 405, 2206  
Rivinius T., Carciofi A. C., Martayan C., 2013, A&A Rev., 21, 69  
Runacres M. C., Owocki S. P., 2002, A&A, 381, 1015  
Sidoli L., Pellizzoni A., Vercellone S., Moroni M., Mereghetti S., Tavani M., 2006, A&A, 459, 901  
Sierpowska-Bartosik A., Torres D. F., 2009, ApJ, 693, 1462  
Smith A., Kaaret P., Holder J., Falcone A., Maier G., Pandel D., Stroh M., 2009, ApJ, 693, 1621  
Strüder L. et al., 2001, A&A, 365, L18  
Takahashi T. et al., 2007, PASJ, 59, 35  
Vladimirov A. E. et al., 2011, Computer Physics Communications, 182, 1156  
Vovk I., Neronov A., 2013, ApJ, 767, 103  
Zamanov R., Stoyanov K., Martí J., Tomov N. A., Belcheva G., Luque-Escamilla P. L., Latev G., 2013, A&A, 559, A87  
Zdziarski A. A., Neronov A., Chernyakova M., 2010, MNRAS, 403, 1873